HHS Public Access

Author manuscript

Ultrasound Med Biol. Author manuscript; available in PMC 2022 August 01.

Published in final edited form as:

Ultrasound Med Biol. 2021 August ; 47(8): 2296–2309. doi:10.1016/j.ultrasmedbio.2021.03.035.

Microbubble-Enhanced Heating: Exploring the Effect of Microbubble Concentration and Pressure Amplitude on High Intensity Focused Ultrasound Treatments

Alicia Clark[1], **Sierra Bonilla**[1], **Dingjie Suo**[1], **Yeruham Shapira**[2], **Michalakis Averkiou**[1]

[1]Department of Bioengineering, University of Washington, Seattle

[2]InSightec, Haifa, Israel

Abstract

High intensity focused ultrasound (HIFU) is a noninvasive tool that can be used for targeted thermal ablation treatments. Currently, HIFU is clinically approved for treatment of uterine fibroids, various cancers, and certain brain applications. However, for brain applications such as essential tremors, HIFU can only be used to treat limited areas confined to the center of the brain due to geometrical limitations (shape of the transducer and skull). A major obstacle for advancing this technology is the inability to treat non-central brain locations without causing damage to the skin and/or skull. Previous research has shown that cavitation-induced bubbles or microbubble contrast agents can be used to enhance HIFU treatments by increasing ablation regions and shortening acoustic exposures at lower acoustic pressures. However, there has been little research done to explore the interplay between microbubble concentration and pressure amplitude on HIFU treatments. We developed an *in-vitro* experimental setup to study lesion formation at three different acoustic pressures and three microbubble concentrations. Real-time ultrasound imaging was integrated to monitor initial microbubble concentration and subsequent behavior during the HIFU treatments. Depending on the pressure used for the HIFU treatment, there was an optimal concentration of microbubbles that led to enhanced heating in the focal area. If the concentration of microbubbles was too high, the treatment was detrimentally affected due to nonlinear attenuation by the pre-focal microbubbles. Additionally, the real-time ultrasound imaging provided a reliable method to monitor microbubble activity during the HIFU treatments, which is important for translation to *in vivo* HIFU applications with microbubbles.

Keywords

high intensity focused ultrasound; ultrasound contrast agents; bubble enhanced heating; acoustic shadowing; inertial cavitation

Corresponding Author: Michalakis A. Averkiou, Department of Bioengineering, University of Washington, Box 355061, N107 William H. Foege Building, 3720 15th Ave NE, Seattle, WA 98195-5061; maverk@uw.edu, Telephone: (206) 616-9558.

INTRODUCTION

High intensity focused ultrasound (HIFU) is a noninvasive tool for targeted thermal ablation treatments that is used clinically for treatment of various cancers and uterine fibroids (Dubinsky et al. 2008; Miller et al. 2012). Additionally, it has applications in the brain for treatment of essential tremor (Elias et al. 2016; Gallay et al. 2016; Lipsman et al. 2013), Parkinson's disease (Magara et al. 2014; Schlesinger et al. 2015), and neuropathic pain (Jeanmonod et al. 2012; Martin et al. 2009). Current HIFU treatments in the brain require very high acoustic intensities for treatment since a large amount of energy is absorbed or reflected by the skull. With current available technology (Ex Ablate 3000, InSightec, Haifa, Israel), focused ultrasound is only capable of burning small regions (~1-2 mm in diameter) in the center of the brain. Safely increasing the ablation zone to more quickly treat larger areas and decreasing the acoustic intensity to limit skull/skin burns is necessary to treat more areas of the brain, allowing for treatment of a wider range of neurological disorders.

Previous research has shown that HIFU in conjunction with gas-filled bubbles can increase ablation regions and shorten acoustic exposures at lower acoustic pressures. Holt and Roy (2001) used two different types of tissue-mimicking phantoms, a polyvinyl alcohol (PVA) and agar phantom, to explore the role of bubbles in enhancing heating by varying acoustic pressure and insonation duration. They did not directly introduce microbubbles into their phantoms. Instead, they induced bubbles through cavitation in the phantoms. They observed that there was a significant temperature rise once a certain critical pressure amplitude (inertial cavitation threshold) was reached. Tung et al. (2006) studied microbubble-enhanced heating in polyacrylamide (PAA) phantoms embedded with different concentrations of Definity microbubbles (Lantheus Medical Imaging, N. Billerico, MA). They observed that microbubbles enhanced the heating in phantoms and reduced the power required to form a lesion by about 30%. They also saw an increase in lesion size and shift in lesion location when microbubbles were added to the phantom. They hypothesized that the Definity microbubbles act as nucleation sites that reduce the threshold of inertial cavitation and thus contribute to heating enhancement.

Ex vivo experimental studies have also been performed to better understand bubble enhanced heating. Clarke and ter Haar (1997) conducted experiments in cow, pig, and lamb liver tissues and dog prostate tissue at a range of pressures. They observed that, when cavitation was induced in the tissues, there was a sudden increase in temperature. Additionally, at the highest power levels that they tested, there was a rapid drop in temperature after the initial temperature increase, which they proposed was due to the area of maximum heating moving forward as the lesion propagated closer towards the transducer. Inspired by this and other previous work, Fujishiro et al. (1998) conducted experiments in excised beef liver that was injected with a first-generation contrast agent, Albunex (Molecular Biosystems, San Diego, CA). They observed that the microbubbles doubled the temperature rise in the liver specimen. Bailey et al. (2001) also performed experiments in excised beef liver to explore the role of bubbles on lesion shape. They concluded that cavitation bubbles were responsible for making tadpole-shaped, instead of cigar-shaped, lesions.

In addition to *ex vivo* experiments, many *in vivo* experiments have also looked into bubble-enhanced heating. Here we highlight some of these experimental contributions. Hynynen (1991) performed experiments in a dog thigh at a range of frequencies and pressures. He saw a sudden increase in temperature when cavitation activity was present, suggesting that bubbles may act to enhance heating in thermal treatments. Additionally, he first observed that a brighter hyperechoic region, which correlated to the region being ablated, appeared in ultrasound images. Sokka et al. (2003) induced cavitation in rabbit thighs to create gas bubbles at the focus of the HIFU treatment transducer. They showed that lesions created while there were cavitation bubbles are approximately 3 times larger than lesions created without these bubbles. Additionally, they showed that there are faster temperature rises and higher measured temperatures with bubbles. Other studies also showed that HIFU-induced lesions were larger in animals given microbubbles (Kaneko et al. 2005; Yu et al. 2004; Yu et al. 2006), that temperature increases in the animals treated with microbubbles were also higher (Kaneko et al. 2005; Umemura et al. 2005), and that adding microbubbles lead to shorter treatment durations and lower power requirements (Tran et al. 2003; Yu et al. 2004; Yu et al. 2006).

McDannold et al. (2006) performed similar work on rabbit brains. They showed that microbubbles enhance heating and reduce power requirements for lesion formation in the brain. McDannold et al. (2016) extended the use of microbubbles for lesion formation to evaluate the long-term effects of nonthermal ablation (with the use of contrast agent microbubbles) in the brain using a rat model. They showed that there were no unexpected, delayed effects due to the ablation treatment, which is encouraging for this technology for future brain applications.

The work in tissue-mimicking phantoms and *ex vivo* and *in vivo* animal models mentioned above highlight the potential of microbubbles in clinical HIFU ablation treatments, especially related to brain applications. These studies show that inducing cavitation bubbles or adding contrast agent microbubbles to HIFU treatments has many benefits such as increased lesion size and decreased treatment duration; however, there is still a gap in the literature related to whether bubble-enhanced heating can occur at lower pressure amplitudes where inertial cavitation is not present, which could lead to a more controlled treatment. There is also a need for further exploration of the relationship between microbubble concentration and pressure amplitude during HIFU treatments. We, therefore, studied microbubble-enhanced heating in a tissue-mimicking egg white phantom under real-time ultrasound image-guidance. We carefully monitored microbubble concentration and behavior (as observed from scattering under imaging conditions) both during the phantom preparation process and during the HIFU exposure using real-time ultrasound imaging in order to get a better understanding of bubble-enhanced heating. We also performed temperature measurements, using thin-wire thermocouples, both with and without microbubbles to monitor the temperature rise during the HIFU treatment.

MATERIALS AND METHODS

Egg white gel phantoms

Egg white polyacrylamide gel phantoms were used to study the influence of microbubble concentration and pressure amplitude on HIFU ablation treatments. Polyacrylamide tissue-mimicking phantoms were first introduced for diagnostic applications since they had similar acoustical and physical properties to tissue (Lafon et al. 2001; Lafon et al. 2005; Takegami et al. 2004). An optically transparent polyacrylamide phantom containing egg white was used for the current work since it was low cost and performed well in previous HIFU studies (Takegami et al. 2004; Tung et al. 2006). The egg white acted as a temperature indicator since it denatured at a fixed temperature and turned white in the denatured area, which allowed for visual observation of any observed lesions created by the HIFU treatments. The size of the phantom was 40x40x70 mm and it was placed 42 mm away from the HIFU transducer such that the geometric focus of the transducer was roughly at the center of the phantom at 20 mm from its edge (see Figure 2a). The acoustic properties of the phantoms, speed of sound, density and attenuation were measured for every phantom and small variations were observed.

Four different types of microbubbles were evaluated for dilution into the egg white phantoms: an in-house “Definity-like” microbubble (De Cock et al. 2015; De Temmerman et al. 2011) which we will refer to as Bubble-G, Optison (GE Healthcare Inc., Princeton, NJ), Sonovue (Bracco Imaging, Milan, Italy), and Sonazoid (GE Healthcare Inc., Princeton, NJ). The Bubble-G microbubbles, composed of DPPC (1,2-dipalmitoyl-sn-glycero-3-phosphocholine) and DSPE-PEG (1,2-distearoyl-sn-glycero-3-phosphoethanolamine-N-[methoxy(polyethylene glycol)-2000]) (Avanti Polar Lipids Inc, Alabaster, AL) in a 95:5 molar ratio, were prepared as previously described in De Cock et al. (2015). The commercial microbubbles were prepared according to the instructions on their packaging. The microbubbles were then carefully diluted into degassed, deionized water until the desired concentration was obtained.

Once the microbubble/water solution was prepared and before mixing it into the phantoms, we observed the concentration of the microbubbles in the solution using contrast-enhanced ultrasound (CEUS) imaging, a nonlinear imaging method that helps to isolate microbubbles based on their nonlinear response (Averkiou et al. 2020b). The intensity of the microbubbles was quantified in the CEUS images by finding the average intensity in a selected region of interest (ROI) with the QLAB quantification software (Philips Healthcare, Bothell, WA). This allowed us to correlate image intensity with microbubble concentration; the higher the image intensity, the higher the concentration of microbubbles (Lampaskis and Averkiou 2010). Next, the microbubbles were diluted into the egg white phantoms. Each type of microbubble was diluted into a separate egg white phantom.

CEUS images of the egg white phantom with different microbubble dilutions were taken with the L9-3 probe of the Philips iU22 ultrasound system (Philips Healthcare, Bothell, WA). As the concentrations of microbubbles increased, so did the image intensity (Figure 1). Table 1 shows whether or not the diluted microbubbles were present in the prepared egg white phantom. The Bubble-G microbubbles and Optison were not present in the prepared

phantom when scanning with contrast-enhanced ultrasound; therefore, these microbubbles were not used in this study. The Sonovue and Sonazoid microbubbles were present in the prepared egg white phantoms. The dilution of the Sonazoid microbubbles into the phantoms was more consistent and reproducible. Small microbubble concentration variations were recorded from batch to batch (and often from vial to vial) but with the procedure described above we confirmed consistent relative concentrations within a batch. Consequently, Sonazoid microbubbles were used to further study microbubble-enhanced heating in egg white phantoms.

Once Sonazoid was selected as the contrast agent to use in the studies, three different concentrations of Sonazoid microbubbles were diluted into the egg white phantoms. At the lowest concentration of microbubbles (~10^2 MBs/mL), a small number of microbubbles can be seen in the phantom (orange dots in the image) (Figure 1(a)). As the concentration of microbubbles is increased (10^3 MBs/mL and 10^4 MBs/mL), more microbubbles appear in the contrast-enhanced ultrasound images (Figure 1(b)-(c)). To further confirm that microbubbles were present in the phantoms, the mechanical index (MI), proportional to the peak negative pressure of the HIFU transducer, on the iU22 ultrasound system was increased until the microbubbles were destroyed in the transducer path. Microbubbles in the path of the imaging probe were uniformly eliminated in the phantom at MI>0.2, creating an image where only the thermocouple was seen. This procedure also confirmed that the bubbles in the gel phantom, despite being confined and not able to move, still possessed the similar scattering and destruction properties.

Experimental setup

Figure 2 shows a schematic (a) and a photograph (b) of the experimental setup used for studying microbubble enhanced heating in an egg white phantom under real-time image guidance. A focused single element circular transducer (diameter = 64.0 mm, focal distance = 63.2 mm, frequency = 0.9 MHz) (H-116, Sonic Concepts, Seattle, WA, USA) was used as the ultrasound source. A 40G thin-wire thermocouple (5TC-TT-T-40-36, Omega Engineering Inc., Norwalk, CT, USA) was inserted into the center of the 40x40x70 mm egg white phantom which was placed 42 mm away from the HIFU transducer to take temperature measurements; the wire tip of the thermocouple extended approximately 2 mm from the PFA shaft. This very thin thermocouple was chosen to reduce thermocouple artifacts (Hynynen and Edwards 1989; Morris et al. 2008). An L9-3 imaging probe from a Philips iU22 diagnostic ultrasound scanner (Philips Healthcare, Bothell, WA) was placed perpendicular to the ultrasound transducer to provide real-time monitoring of the HIFU treatment.

The L9-3 imaging probe was aligned to the thermocouple using a three-axis positioning system. The alignment was performed by maximizing the intensity of the thermocouple in the ultrasound images. The bright echo produced by the thermocouple in Figure 1 is due to beamformer saturation and incomplete linear signal cancellation in the nonlinear amplitude modulation mode (Averkiou et al. 2020b). The focus of the HIFU transducer was next aligned to the tip of the thermocouple using the pulse echo method. Pulse echo measurements were recorded from the oscilloscope using a custom LabVIEW virtual

instrument (National Instruments, Austin, TX). An image was created from these pulse echo measurements that allowed the thermocouple tip to be easily located, and the error in localizing the tip was found to be approximately ±1 mm. This error is similar (perhaps slightly greater) to what has been reported in the literature (Holt and Roy 2001). However, our experimental set up has the additional complexity of co-aligning also the ultrasound probe with the thermocouple and the focus of the HIFU source. Additionally, low pressure amplitudes (<0.05 MPa) were used for the pulse echo measurements to minimize the effects of the sound field on the microbubbles in the phantom. We have considered adding a passive cavitation detection system (Keller et al. 2020) to also monitor inertial cavitation. However, we felt that this added experimental complexity could be avoided since we had accurate values for the inertial cavitation threshold of Sonazoid and all the amplitudes used in our work were well above that value; and we already had real-time ultrasound imaging. When bubbles are in a confining viscoelastic medium the threshold of inertial cavitation can be greater than when they are in a liquid (Dollet, et al. 2019, Yang and Church 2005) and this may be more likely for the 0.5 MPa pressure. However, we also note that bubble destruction thresholds were similar in water and the egg white phantoms and we assume that the inertial cavitation thresholds were similar too. (Radhakrishnan, et al. 2013)

Experimental protocol

Experiments were conducted in the egg white phantoms at three different concentrations of Sonazoid microbubbles: low (10^2 MBs/mL), medium (10^3 MBs/mL), and high (10^4 MBs/mL) and at three different pressure amplitudes: 0.5 MPa, 2.0 MPa, and 6.0 MPa. These pressure amplitudes corresponded to the focal pressure amplitudes recorded in water with a membrane hydrophone (UT1604-225, Precision Acoustics, Dorchester, UK). In actuality, the focal pressure inside the phantom when attenuation is accounted for was slightly lower than the water focal values noted here. However, for simplicity we will refer to the water focal values throughput the manuscript. For each experiment, the egg white phantom was treated with the H-116 HIFU transducer for 30 seconds at an 82% duty cycle to allow ultrasound imaging to be interleaved with the HIFU treatment. During this 30 second interval, the ultrasound was on for 411.1 milliseconds (370,000 ultrasound cycles) followed by an 88.9 millisecond period where a diagnostic image was taken, as demonstrated in Figure 3. This procedure was repeated throughout the entire 30 second treatment duration. The interleaved imaging was used to monitor the behavior of the microbubbles diluted in the phantom and monitor for lesion formation. Thermocouple temperature measurements were recorded every 0.1 s (10 Hz sampling rate) during the entire 30 second treatment time and an additional 30 seconds afterwards to monitor the phantom as it returned to ambient temperature.

Characterization of the HIFU transducer

To characterize the H-116 single element transducer and confirm its dimensions, we measured its axial (propagation curve) and focal lateral field (beam pattern) in an ultrasonic water tank with a 0.4 mm sensor diameter polyvinylidene fluoride (PVDF) membrane hydrophone (UT1604-225, Precision Acoustics, Dorchester, UK) calibrated in the 0.5-30 MHz range. LabVIEW virtual instruments were used to control the 3D positioning of the membrane hydrophone and to record the voltage membrane hydrophone measurements. We

compared the hydrophone measurements with theoretical predictions based on the Rayleigh integral, as shown in Figure 4. We fitted the hydrophone measurements to the theoretical predictions by making small adjustments to the focal depth and diameter provided by the manufacturer. The best fit was obtained for focal depth of 62.1 mm and diameter of 58.2 mm (the manufacturer supplied values were 63.2 mm and 64.0 mm, respectively). In addition, we confirmed the width (~2.5 mm) and length (~15.8 mm) of the focal volume (region where the acoustic pressure is within ½ the maximum value).

Ultrasound Imaging Parameters

We used a contrast specific imaging mode on the Philips iU22 ultrasound system and collected images with the L9-3 linear array probe. A dual side-by-side image format was used, where a contrast image obtained using a nonlinear technique (3.1 MHz, amplitude modulation) is displayed on the left and a conventional B-mode image (5 MHz, fundamental imaging) is displayed on the right (Averkiou et al. 2020b). To avoid bubble destruction, both images were acquired at low MI (<0.08). Typically, in clinical scanning, microbubbles are displayed in the contrast image and tissue in the B-mode image. In our phantom images here, nonlinear echoes from resonant microbubbles were displayed in the contrast image, and linear echoes from larger (outside resonant size) gas bubbles were displayed in the fundamental B-mode image. The frame rate was 2 Hz selected by the manual triggering option in order to allow for the interleaving of the HIFU ultrasound exposure as described above and in Figure 3.

Image Post-Processing

DICOM files were post-processed using MATLAB (MathWorks, Natick, MA). The DICOM files were loaded into MATLAB using built-in DICOM functions. After the images were imported, background subtraction was performed on the images. An image of the phantom before the HIFU transducer was turned on was used as the background image. This image was then subtracted off of the subsequent frames to look at changes that occurred throughout the DICOM loop. For example, if microbubbles undergo expansion during the HIFU exposure, there would be greater signal intensity in the subsequent ultrasound images than in the background image, which became more obvious by background subtraction. Likewise, if microbubbles were destroyed in the subsequent images, there would be a clear loss of signal intensity in the background subtracted images.

Additional analysis was performed on the DICOM loops using QLAB (Philips Healthcare, Bothell, WA). The linearized intensity of the images over time in a region of interest (ROI) was analyzed using the built-in ROI feature to quantify the amount of bubble destruction.

RESULTS

Ultrasound Imaging Results

Figure 5 shows ultrasound images taken for three different microbubble concentrations at 2.0 MPa. These images are shown at different time points during the HIFU treatment: t = 0 seconds was recorded before the HIFU treatment was started (Figure 5 (a), (e), (i)), t = 0.5 seconds was taken after the first pulse of 370k cycles (Figure 5 (b), (f), (j)), t = 15.5 seconds

occurred halfway through the HIFU treatment (Figure 5 (c), (g), (k)), and t = 30.5 seconds was recorded immediately after the HIFU transducer was turned off (Figure 5 (d), (h), (l)). Ultrasound from the H-116 propagated from left to right in the images, and the focus of the ultrasound field was aligned to the tip of the thermocouple (appearing as a bright echo in the center of the images) using the pulse echo techniques described previously. At the lowest concentration of microbubbles used in the experiments, microbubbles in the HIFU beam path were immediately destroyed after the first ultrasound cycle. There is a noticeable void in the contrast image in front of and around the thermocouple at 0.5 seconds (Figure 5(b)). Additionally, the fundamental image at 0.5 seconds in Figure 5(b) shows that larger (non-resonant) gas bubbles, appearing as hyperechoic regions, were produced by the HIFU. The hyperechoic region (area of increased intensity) in the fundamental image also shows the symmetry in the ultrasound field at this low microbubble concentration. As time progresses, more microbubbles were destroyed; however, the hyperechoic region was present even after the treatment finished (Figure 5(c)–(d)). This region slowly dissolved over time depending on the concentration of microbubbles and HIFU amplitude used. At lower pressures and concentration, the region dissolved in about an hour and at higher pressures and concentration it was still visible even after 24 hours.

The behavior of the microbubbles at the medium concentration at 2.0 MPa is different than at the lower concentration of microbubbles, as seen in the contrast images at t = 0.5 and 15.5 seconds (Figure 5(f)–(g)). While many of the microbubbles in the beam path were still destroyed, there is now sustained cavitation activity occurring around the periphery of the HIFU beam which corresponds to the increase in intensity in this peripheral area in the contrast images. Additionally, there is a region of sustained microbubble cavitation activity directly in front of the thermocouple tip (Figure 5(g)), which is further quantified using a region of interest (ROI) analysis in Figure 7 (discussed in more detail below). In the fundamental B-mode image at 0.5 seconds (Figure 5(f)), there are noticeably less larger gas bubbles formed post-focally compared to at the lower concentration of microbubbles (Figure 5(b)). This asymmetry in the hyperechoic region is due to nonlinear microbubble attenuation of the sound field. In response to the incoming HIFU beam, the microbubbles oscillate in size. When the microbubbles increase in size, they allow little ultrasound energy to transmit through them, effectively acting as a shield. Finally, after the ultrasound is turned off (Figure 5(h)), there was no longer microbubble cavitation activity occurring, and there were no longer any noticeable areas of increased intensity around the beam periphery or in front of the thermocouple in the contrast image.

At the highest concentration of microbubbles, there is similar peripheral enhancement in the contrast images (Figure 5(i)–(j)) as in the images for the medium concentration of microbubbles. Interestingly, for this higher concentration, the pre-focal microbubbles were still present in the contrast images and were not immediately destroyed at 0.5 seconds (Figure 5(i)), possibly due to the increased number of microbubbles present and increased attenuation. In these contrast images, there were also microbubbles still present in the beam path after the ultrasound was turned off (Figure 5(l)); however, the majority of these microbubbles disappeared a few seconds after completion of the HIFU treatment. The shape of the hyperechoic region in the fundamental images does not change significantly during the treatment duration for this microbubble concentration (Figure 5(j)–(l)). The attenuation

due to the high microbubble concentration is causing the asymmetry between prefocal and postfocal regions seen in the fundamental images in Figures 5(j)–(l). This asymmetry is more pronounced here than at the lower concentrations of microbubbles. Similar observations were made with the lower and higher pressures (0.5 and 6 MPa) and the complete video loops of all 9 pressure-concentration combinations are provided as supplemental material.

Image Post-Processing

Often, further post-processing of ultrasound images helps to bring certain imaging details into focus. For our work here, we identified that emphasizing bubble activation and destruction would be important. The images before the HIFU transducer was turned on (Figure 5(a), (e), (i)) were subtracted from the images taken after 0.5 seconds of ultrasound exposure at 2 MPa (Figure 5(b), (f), (j)) to form the images shown in Figure 6. It is important to note that only the regions of the image that are enhanced (the intensity in the image increases) between 0 seconds and 0.5 seconds are shown in the figure. The background subtracted images help to visualize cavitation activity occurring immediately after the first HIFU pulse. The contrast-enhanced background subtracted images (Figure 6(a), (c), (e)) show resonant (nonlinear) bubble activity, whereas, the fundamental B-mode background subtracted images (Figure 6(b), (d), (f)) show linear scattering from larger gas bubbles that do not produce nonlinear signals. It is interesting to note that there is noticeable nonlinear microbubble activity at the periphery of the HIFU beam at all microbubble concentrations in the background subtracted contrast images (Figure 6(a), (c), (e)). This enhancement was difficult to observe visually in the images of Figure 5, especially at the lowest microbubble concentration. The effect of nonlinear microbubble attenuation is shown in the fundamental B-mode images (Figure 6(b), (d), (f)). As the microbubble concentration is increased, the hyperechoic region (assumed to be the result of linear scattering from larger bubbles) in the fundamental images, now highlighted in the background subtracted fundamental images, loses its symmetry due to attenuation of the incoming ultrasound beam by the microbubbles. Finally, the black linear void in these images represents the location of the thermocouple which was eliminated by the background subtraction process.

Next, QLAB and MATLAB were used to further study the behavior of the microbubbles at the medium concentration of microbubbles at 2.0 MPa since we observed that there was a region of increased brightness directly in front of the thermocouple tip in the contrast-enhanced ultrasound images. A region of interest (ROI) analysis was performed using QLAB to study the behavior of the microbubbles in this region. The selected ROI is shown in green in Figure 7(a). The ROI is displayed on the image taken at 19 seconds, corresponding to the time point where the intensity is maximum in the ROI (highlighted by a vertical white line in Figure 7(c)). Figure 7(b) shows a background subtracted contrast-enhanced ultrasound image for the medium concentration of microbubbles at 2.0 MPa. Background subtraction was performed in MATLAB between the DICOM images at 0 seconds (Figure 5(e)) and 19 seconds (Figure 7(a)). The previous background subtraction scheme (Figure 6 (a)–(f)) only highlighted regions where microbubbles were present or oscillating, but the background subtraction scheme used for this analysis allowed visualization of the regions where microbubbles were present (shown in white) as well as

regions where microbubbles were destroyed/not present (shown in purple). Finally, the intensity in the ROI region as a function of time is shown in Figure 7(c) for the HIFU treatment. As the treatment progressed, the intensity of the ultrasound image in that region increased, showing that there was sustained microbubble activity (assumed to be inertial cavitation since the acoustic pressure used is well above the inertial cavitation threshold of Sonazoid as recently published (Keller et al. 2020), with every HIFU pulse in that region for the duration of the treatment.

Finally, QLAB was used to monitor the effect of the HIFU treatment (mainly bubble destruction) on the microbubbles outside of the main beam path for all pressures at the medium concentration of microbubbles. The linearized intensity of the ROI outside of the main beam path (Figure 8(a)) is plotted as a function of time in Figure 8(b) for the 3 pressures. The intensity is normalized with respect to the maximum intensity seen in the ROI over the treatment duration. At the lowest pressure (0.5 MPa), there is little microbubble destruction in the ROI as observed from the low slope of the intensity-time curve. The decrease in intensity throughout the HIFU treatment is partly due to some minimal bubble destruction from the L9-3 imaging probe and to the natural decay of the microbubbles. At 2.0 MPa, there was a noticeable drop in signal intensity after the HIFU transducer was turned on because some microbubbles were immediately destroyed. This destruction is difficult to observe visually as seen when comparing the contrast images in Figure 5(e) and 5(f). After the HIFU treatment concluded, the decay in signal (the slope of the intensity-time curve) was again due to destruction by the L9-3 imaging probe and to the natural decay of the microbubbles. Finally, at the highest pressure (6.0 MPa), there was an even greater decay in the microbubble signal after the HIFU treatment was started. Between 8 and 20 seconds the microbubble signal in the ROI increased. This may be attributed to either microbubble activation at the edge of the ROI from the previous HIFU pulse or signal interference from the strong scattering at the focus being misregistered. After the treatment concluded, there was no noticeable change in microbubble signal, due to the fact that the majority of the microbubbles in the ROI were destroyed.

Temperature Measurements

After discussing the acquired image loops and how they explain the underlying physical principles of bubble enhanced heating, here we present our thermocouple measurements. Figure 9 shows the temperature rise measured with the thermocouple in the egg white phantoms at different concentrations of microbubbles and different pressure amplitudes. The temperature is recorded for a 60 second period: 30 seconds during the HIFU treatment and 30 seconds after the treatment to observe the temperature reduction. At 0.5 MPa, Figure 9(a), the temperature rise at the focus in the phantoms is larger when microbubbles are present than when no microbubbles are present. For the no bubbles case we show the average (dark black line) and the standard deviation (grey shaded region) from 3 measurements. This same trend is not seen at the lowest concentration of microbubbles (10^2 MBs/mL); however, this discrepancy is believed to be due to misalignment of the thermocouple tip to the transducer focus.

In Figure 9(b), we show the temperature rise when the focal pressure is 2 MPa. The line and corresponding shaded area show the average and standard deviation, over 3 different experimental trials, when no bubbles are present (black) and at the low concentration of MBs (10^2 MBs/mL, purple). For the higher bubble concentrations (10^3 and 10^4 MBs/mL, blue and green lines, respectively), acoustic shadowing limits the maximum temperature (as also confirmed in the supplemental videos). There is not a significant temperature rise at the focus itself at 10^4 MBs/mL (green line). Additionally, we observe that the presence of microbubbles at an optimal concentration (for this pressure 10^2 MBs/mL) results in greater temperature rise than when microbubbles are not used. At 6.0 MPa, Figure 9(c), there were large oscillations in the temperature measurements in the first 5-10 seconds of the HIFU treatment at the low and no microbubble concentrations. These oscillations were due to inertial cavitation in the phantom that led to a lesion formation at the focus within 3 s. The lesions extended towards the HIFU transducer with time and reached the outer edge of the phantom by the end of the 30 s exposure (as confirmed by ultrasound imaging). As the microbubble concentration was increased (blue and green curves from 3 measurements and with their respective standard deviation shown as shaded area in the curves), the temperature rise measured with the thermocouple at the focus, was lower than at the lower concentrations of microbubbles.

Figure 9(d) shows temperature measurements taken at two locations along the HIFU beam path at the 2 higher concentrations of microbubbles at 6.0 MPa. The focal thermocouple temperature measurement is the same as shown in Figure 9(c). The front thermocouple temperature measurement was taken at the front face of the phantom (42 mm away from the HIFU transducer) where the ultrasound enters and where lesion formation occurred (see Figure 10(c) below). The temperature rise measured by the focal thermocouple is small (20°C for 10^3 MBs/mL and 2°C for 10^4 MBs/mL); however, there is a significant temperature rise, approximately 50°C for 10^3 MBs/mL and 70°C for 10^4 MBs/mL, measured by the front thermocouple where the acoustic pressure was considerably lower than the focus (the water pressure there is about 1 MPa). The large temperature rise at this front location can be attributed to bubble enhanced heating since the actual pressure at the frontal plane of the phantom was only around 1.0 MPa (determined using the propagation curve of the HIFU transducer, Figure 4(b)); a pressure of 1.0 MPa is not sufficient to cause a significant temperature increase without microbubbles. Additionally, due to the high microbubble concentration, there was no significant temperature increase measured by the focal thermocouple. The high concentration of microbubbles had significantly attenuated the incoming pressure beam.

Lesion Formation

After presenting our images of the bubble enhanced heating process and our thermocouple measurements, here we present the results on lesion size and location. While there were noticeable temperature rises at the different treatment pressures, visible lesions were only formed in the 6.0 MPa phantoms. There were no visible lesions created at 0.5 MPa or 2.0 MPa, mainly due to the overall duration of the treatment. Figure 10 shows the lesions that were formed in these phantoms at 6.0 MPa for the three different microbubble concentrations. At the lowest microbubble concentration (10^2 MBs/mL), a tadpole-shaped

lesion was formed at the thermocouple tip, where the focus was located (Figure 10(a)). The creation of this tadpole-shaped lesion was due to both thermal and mechanical events occurring during the HIFU treatment (Bailey 2001, Chen 2003). The location of the lesion shifted prefocally, closer to the HIFU transducer, at the higher concentrations of microbubbles (10^3 and 10^4 MBs/mL). At the medium concentration of microbubbles (10^3 MBs/mL), the lesion started to form approximately 5 mm before the focus (Figure 10(b)). The shape of the lesion also changed at this microbubble concentration; the lesion was now wider (from top of the image to bottom of the image) than the lesion formed at the lowest concentration of microbubbles. Likewise, at the highest microbubble concentration (10^4 MBs/mL), the lesion started to form even further from the focus, and it was also approximately 3 times wider than at the lowest microbubble concentration (Figure 10(c)). Here we again note that the lesions have been formed at much lower pressures than the intended 6 MPa at these pre-focal locations due to acoustic shadowing (confirmed by imaging). Tung et al. (2006) also observed that the start location of the lesion was dependent on the concentration of microbubbles used for the experiment but much higher pressures (9-12 MPa).

DISCUSSION

Real-time ultrasound imaging together with thermocouple temperature measurements were used to study the effect of acoustic pressure amplitude and microbubble concentration on bubble-enhanced heating in HIFU applications. We found that the location and amount of the delivered thermal dose strongly depended on both the concentration of microbubbles and the pressure amplitude used. Keller et al. (2020) also demonstrated a microbubble concentration- and pressure-dependent attenuation using both hydrophone measurements and detailed high frame rate imaging. A nonlinear relationship between concentration, acoustic amplitude, and attenuation greatly impacted the amount of enhanced heating produced in the focal area in the present study.

By interleaving imaging with the HIFU exposure protocol we have been able to observe the complex bubble behavior immediately after every HIFU pulse. Our imaging observations are derived from 2 different modes (nonlinear/AM and linear/fundamental imaging) which provide complimentary information. We note that imaging is performed immediately after every HIFU pulse in the 0-89 ms time window needed to complete 1 frame and also that the imaging frequencies (3.1 MHz and 5 MHz, for AM and fundamental, respectively) are different from the HIFU frequency (0.9 MHz). The dynamic and complex spatial distribution (due to the nonlinear bubble attenuation) of the supplied HIFU field results in a complex bubble activity that includes bubble growth (with the higher-pressure pulses), destruction, and gas diffusion. The imaging modes are providing that activity immediately afterwards for a single frame. The AM images provide information on the activity of the resonant cavities (resonant here used in a broad sense since imaging is performed with short pulses which induce only a transient response) producing nonlinear scattering, whereas the fundamental images provide information of the larger cavities present that do not produce nonlinear scattering.

Most previous research on bubble-enhanced heating was done without the addition of microbubbles with the exception of only few that used contrast agent microbubbles. Tung et al. (2006) also used a phantom with microbubbles diluted in it while using much higher pressures (9-15 MPa water pressure versus 0.5-6 MPa in the present manuscript) and seemingly much higher concentrations. Their results indirectly suggest the nonlinear bubble attenuation without clearly demonstrating it as we were able to do with the ultrasound imaging in the present work. They also point out the need for a real-time imaging technique to translate this technique in vivo, which partly motivated the present work.

For the experiments conducted at 0.5 MPa, there was only a small temperature increase (>5°C) for any concentration of microbubbles. This suggests that there is a pressure threshold, that must be reached before this technique would be useful for ablative treatments. It is worth noting that the phantoms with the microbubbles did experience greater temperature elevations than the phantom without microbubbles even at this low pressure. While this may not be useful for ablative treatments, it could potentially be helpful in mild hypothermia applications. Additionally, at 0.5 MPa, there is still observable microbubble attenuation at the highest concentration of microbubbles, although the beam still preserves some of its symmetry, unlike at the higher-pressure amplitudes. It could be interesting to repeat these experiments at a higher concentration of microbubbles to see if higher concentrations of microbubbles are needed to obtain a more significant temperature elevation at this pressure.

At the intermediate pressure (2.0 MPa), microbubbles play a more important and also complex role on bubble-enhanced heating. For the low concentration of microbubbles, there is a noticeable temperature increase compared to the phantom without microbubbles. At the medium microbubble concentration, there is still a very small increase in temperature measured at the focus compared to the temperature measured when the phantom did not contain microbubbles. However, the slope of the temperature elevation changes, which we hypothesize is caused due to the attenuation of the ultrasound field by the pre-focal microbubbles. It is very possible that the maximum temperature rise was not at the thermocouple tip which was placed at the focus but instead at a location closer to the transducer. At the highest concentration of microbubbles, the prefocal microbubbles attenuate the pressure field dramatically and cause the heating to occur away from the focus (proximal to the HIFU source) and not at the intended location where we have placed the thermocouple; therefore, there is no noticeable temperature rise at the focus. The attenuation of the ultrasound beam, particularly for the highest microbubble concentration, was also observed via real-time ultrasound imaging (Figure 5(j)–(l)). The hyperechoic region seen in the fundamental images is not symmetric due to the attenuation.

At the highest pressure (6.0 MPa), the temperature rise measured in the phantom with the low concentration of microbubbles was higher than the temperature rise measured in the phantom without microbubbles. However, the measured temperature rises were lower than measured in the phantom without microbubbles at the higher microbubble concentrations. At these higher concentrations, the pre-focal microbubble cavitation greatly reduced the focal amplitude. Consequently, the lesion formation occurred pre-focally as shown in Figure 10(b)–(c). Also, at the highest microbubble concentration, the temperature increased after

the HIFU treatment had concluded due to significant prefocal heating that caused a slight increase in temperature at the focus as heat was conducted through the phantom (Figure 9(c)). Finally, for both of the higher microbubble concentrations, there was still a noticeable temperature rise in the phantom prefocally which was not captured by our thermocouple measurement at the focus. This was supported by Figure 9(d) where the experiment with the 2 higher concentrations was repeated with an additional thermocouple placed at the expected site of lesion formation (at the front face of the phantom). In this pre-focal region, a temperature increase of 50-70°C was observed (Figure 9(d)).

These results demonstrate the complex relationship between bubble-induced attenuation, microbubble concentration, and pressure amplitude during targeted thermal ablation treatments, when the bubbles are diluted uniformly along the path of the HIFU source. Depending on the pressure used for the HIFU treatment, there is an optimal concentration of microbubbles to use for the treatment. If the concentration of microbubbles is too high, the targeting of the treatment area will be misplaced due to nonlinear attenuation by the prefocal microbubbles. This has important clinical implications because it is imperative that clinicians know exactly where in the body heating will be introduced. For example, if the microbubble concentration is too high, the HIFU could ablate the prefocal region, instead of the intended location at the focus, leading to unsuccessful treatment. This demonstrates that real-time ultrasound imaging, including both nonlinear contrast imaging and linear B-mode imaging, to monitor microbubble activity during treatment is paramount for the success of the treatment. The influence of nonlinear attenuation on bubble enhanced heating could be removed with local bubble injections in the tissue only in the vicinity of the treatment area. In this way, the alteration of the HIFU pressure field due to bubble attenuation would be eliminated and the lesions would naturally occur at the focus.

Most previous research has only used fundamental imaging to monitor lesion formation. In this present work, contrast-enhanced ultrasound helped to verify that microbubbles were indeed present in the phantom and allowed us to study the microbubble activity over the course of the treatment. This imaging modality and triggering synchronization will be necessary in translating this technology to the clinic because it allows for monitoring of the microbubbles at the treatment site. It will be extremely important to know that the right concentration of microbubbles is present in the treatment area as the presence and concentration of microbubbles not only affect the temperature rise but also may shift the location and dimensions of the lesion. Furthermore, the use of bolus transit quantification will allow the selection of an optimal concentration of microbubbles to be injected in the clinic by evaluating first the signal intensity for various volumes of microbubble bolus injections (Averkiou et al. 2020a).

It is also important to note here that only measuring the temperature at the focus is a limitation of the current study since the pressure field inside the phantom is dynamic and largely affected by the microbubble concentration. While using more thermocouples could be helpful for future studies, there are still drawbacks to this approach, including increased disruption of the ultrasound field by the increased number of thermocouples and the same difficulty in knowing exactly where to place the thermocouples due to the altered focal area for each pressure amplitude and microbubble concentration. Holt and Roy (2001) placed

their array of thermocouples also oriented parallel to the acoustic axis of the HIFU source like we did, but additionally they have avoided taking temperature measurements exactly at the focus as an attempt to deal with the thermocouple viscous heating artifact which in retrospect seems to be a preferred approach. In future work, it would be best to use a temperature measurement technique that would capture the whole 3D temperature field such as thermal camera imaging, MR temperature measurements, or ultrasound imaging temperature measurement techniques. Unfortunately, there are drawbacks to these methods as well: thermal imaging can only be used for surface temperature measurements and cannot be used to measure a temperature rise inside of the phantom; MR temperature measurements have low temporal resolution and access to MR is limited; and ultrasound temperature measurement techniques are still being actively researched and developed.

An inherent limitation of the present study is the use of a gel phantom with uniformly diluted microbubbles intended for the study of bubble-enhanced heating in tissue. We have confirmed in our methods that these bubbles, despite being fixed in space, exhibit scattering and destruction behavior largely similar to microbubbles in vivo. However, the simplicity of the gel phantoms has allowed us to develop a real-time imaging approach to study this process and to acquire new knowledge on the complex pressure-concentration-attenuation relationship. In vivo work with a machine perfused pig liver model (Izamis et al. 2014) is currently underway.

CONCLUSIONS

The effect of microbubble concentration and pressure amplitude on microbubble enhanced HIFU was investigated in egg white phantoms under real-time ultrasound image guidance. Our results demonstrate the complex relationship between bubble induced attenuation, microbubble concentration, and pressure amplitude during targeted thermal ablation treatments. Bubble-induced attenuation leads to acoustic shadowing and to the formation of thermal lesions away from the intended location (typically the focal region). The work presented here (detailed images and thermocouple temperature measurements) qualitatively demonstrated that there is an optimal concentration of microbubbles for each pressure amplitude. Collectively, the temperature measurements and the acquired ultrasound images give insight into the relevant bubble activity of HIFU treatments. We observed a correlation between sustained cavitation (presumed to be inertial at the amplitudes used) and large temperature rise. However, at low pressure amplitude, bubble-induced attenuation is minimal and only a very small temperature increase was recorded. We also demonstrated the importance of real-time ultrasound imaging (and post processing) for treatment monitoring. Not only does it allow for real-time visualization of lesion formation, but it also displays the associated microbubble activity (presence of bubbles before the treatment and nonlinear echoes during treatment). Bubble specific ultrasound imaging will be especially important for the clinical translation of this work and should be incorporated into research protocols if microbubbles are to be used clinically in HIFU treatments.

Supplementary Material

Refer to Web version on PubMed Central for supplementary material.

ACKNOWLEDGMENTS

This work was partly supported by NIH/SBIR grant 2R44CA213866-02 and by DODCDMRP grant CA160415/PRCRP. We gratefully acknowledge GE Healthcare for the Sonazoid microbubbles used in this study. We thank Javier Grinfeld and Rafi De Picciotto (both with Insightec) for many discussions and suggestions during their visits to Seattle.

REFERENCES

Averkiou M, Juang E, Gallagher M, Cuevas M, Wilson S, Barr R, Carson P. Evaluation of reproducibility of bolus transit quantification with contrast-enhanced ultrasound across multiple scanners and analysis software packages -A QIBA study. Invest Radiol 2020a;55.

Averkiou MA, Bruce MF, Powers JE, Sheeran PS, Burns PN. Imaging Methods for Ultrasound Contrast Agents. Ultrasound Med Biol 2020b;46:498–517. [PubMed: 31813583]

Bailey MR, Couret LN, Sapozhnikov OA, Khokhlova VA, Ter Haar G, Vaezy S, Shi X, Martin R, Crum LA. Use of overpressure to assess the role of bubbles in focused ultrasound lesion shape in vitro. Ultrasound Med Biol 2001;27:695–708. [PubMed: 11397534]

Clarke RL, Ter Haar GR. Temperature rise recorded during lesion formation by high-intensity focused ultrasound. Ultrasound Med Biol 1997;23:299–306. [PubMed: 9140186]

De Cock I, Zagato E, Braeckmans K, Luan Y, de Jong N, De Smedt SC, Lentacker I. Ultrasound and microbubble mediated drug delivery: acoustic pressure as determinant for uptake via membrane pores or endocytosis. J Control Release Elsevier B.V, 2015;197:20–28.

De Temmerman ML, Dewitte H, Vandenbroucke RE, Lucas B, Libert C, Demeester J, De Smedt SC, Lentacker I, Rejman J. MRNA-Lipoplex loaded microbubble contrast agents for ultrasound-assisted transfection of dendritic cells. Biomaterials Elsevier Ltd, 2011;32:9128–9135.

Dollet B, Marmottant P, Garbin V. Bubble dynamics in soft and biological matter. Annu Rev Fluid Mech 2019; 51:331–55.

Dubinsky TJ, Cuevas C, Dighe MK, Kolokythas O, Joo HH. High-intensity focused ultrasound: Current potential and oncologic applications. Am J Roentgenol 2008;190:191–199. [PubMed: 18094311]

Elias WJ, Lipsman N, Ondo WG, Ghanouni P, Kim YG, Lee W, Schwartz M, Hynynen K, Lozano AM, Shah BB, Huss D, Dallapiazza RF, Gwinn R, Witt J, Ro S, Eisenberg HM, Fishman PS, Gandhi D, Halpern CH, Chuang R, Pauly KB, Tierney TS, Hayes MT, Cosgrove GR, Yamaguchi T, Abe K, Taira T, Chang TW. A randomized trial of focused ultrasound thalamotomy for essential tremor. N Engl J Med 2016;375:730–739. [PubMed: 27557301]

Fujishiro S, Mitsumori M, Nishimura Y, Okuno Y, Nagata Y, Hiraoka M, Sano T, Marume T, Takayama N. Increased heating efficiency of hyperthermia using an ultrasound contrast agent: A phantom study. Int J Hyperth 1998;14:495–502.

Gallay MN, Moser D, Rossi F, Pourtehrani P, Magara AE, Kowalski M, Arnold A, Jeanmonod D. Incisionless transcranial MR-guided focused ultrasound in essential tremor: Cerebellothalamic tractotomy. J Ther Ultrasound 2016;4. [PubMed: 26848391]

Holt RG, Roy RA. Measurements of bubble-enhanced heating from focused, MHz-frequency ultrasound in a tissue-mimicking material. Ultrasound Med Biol 2001;27:1399–1412. [PubMed: 11731053]

Hynynen K The threshold for thermally significant cavitation in dog's thigh muscle in vivo. Ultrasound Med Biol 1991; 17:157–169. [PubMed: 2053212]

Hynynen K, Edwards DK. Temperature measurements during ultrasound hyperthermia. Med Phys 1989;16:618–626. [PubMed: 2549354]

Izamis ML, Efstathiades A, Keravnou C, Leen EL, Averkiou MA. Dynamic Contrast-Enhanced Ultrasound of Slaughterhouse Porcine Livers in Machine Perfusion. Ultrasound Med Biol 2014;40:2217–2230. [PubMed: 25023101]

Jeanmonod D, Werner B, Morel A, Michels L, Zadicario E, Schiff G, Martin E. Transcranial magnetic resonance imaging-guided focused ultrasound: noninvasive central lateral thalamotomy for chronic neuropathic pain. Neurosurg Focus 2012;32:1–11.

Kaneko Y, Maruyama T, Takegami K, Watanabe T, Mitsui H, Hanajiri K, Nagawa H, Matsumoto Y. Use of a microbubble agent to increase the effects of high intensity focused ultrasound on liver tissue. Eur Radiol 2005;15:1415–1420. [PubMed: 15739112]

Keller SB, Sheeran PS, Averkiou MA. Cavitation therapy monitoring of commercial microbubbles with a clinical scanner. IEEE Trans Ultrason Ferroelectr Freq Control 2020;3010:1–1.

Lafon C, Kaczkowski PJ, Vaezy S, Noble M, Sapozhnikov OA. Development and characterization of an innovative synthetic tissue-mimicking material for high intensity focused ultrasound (HIFU) exposures. Proc IEEE Ultrason Symp IEEE, 2001;2:1295–1298.

Lafon C, Zderic V, Noble ML, Yuen JC, Kaczkowski PJ, Sapozhnikov OA, Chavrier F, Crum LA, Vaezy S. Gel phantom for use in high-intensity focused ultrasound dosimetry. Ultrasound Med Biol 2005;31:1383–1389. [PubMed: 16223642]

Lampaskis M, Averkiou M. Investigation of the Relationship of Nonlinear Backscattered Ultrasound Intensity with Microbubble Concentration at Low MI. Ultrasound Med Biol 2010;36:306–312. [PubMed: 20045592]

Lipsman N, Schwartz ML, Huang Y, Lee L, Sankar T, Chapman M, Hynynen K, Lozano AM. MR-guided focused ultrasound thalamotomy for essential tremor: A proof-of-concept study. Lancet Neurol Elsevier Ltd, 2013;12:462–468.

Magara A, Bühler R, Moser D, Kowalski M, Pourtehrani P, Jeanmonod D. First experience with MR-guided focused ultrasound in the treatment of Parkinson's disease. J Ther Ultrasound 2014;2:1–8. [PubMed: 25516803]

Martin E, Jeanmonod D, Morel A, Zadicario E, Werner B. High-intensity focused ultrasound for noninvasive functional neurosurgery. Ann Neurol 2009;66:858–861. [PubMed: 20033983]

McDannold N, Zhang Y, Vykhodtseva N. Nonthermal ablation in the rat brain using focused ultrasound and an ultrasound contrast agent: Long-term effects. J Neurosurg 2016;125:1539–1548. [PubMed: 26848919]

McDannold NJ, Vykhodtseva NI, Hynynen K. Microbubble contrast agent with focused ultrasound to create brain lesions at low power levels: MR imaging and histologic study in rabbits. Radiology 2006;241:95–106. [PubMed: 16990673]

Miller DL, Smith NB, Bailey MR, Czarnota GJ, Hynynen K, Makin IRS, Bioeffects Committee of the American Institute of Ultrasound in Medicine. Overview of therapeutic ultrasound applications and safety considerations. J Ultrasound Med 2012;31:623–34. [PubMed: 22441920]

Morris H, Rivens I, Shaw A, Haar G Ter. Investigation of the viscous heating artefact arising from the use of thermocouples in a focused ultrasound field. Phys Med Biol 2008;53:4759–4776. [PubMed: 18701773]

Radhakrishnan K, Bader KB, Haworth KJ, Kopechek JA, Raymond JL, Huang S-L, McPherson DD, Holland CK. Relationship between cavitation and loss of echogenicity from ultrasound contrast agents. Physics in Medicine & Biology 2013; 58:6541. [PubMed: 24002637]

Schlesinger I, Eran A, Sinai A, Erikh I, Nassar M, Goldsher D, Zaaroor M. MRI guided focused ultrasound thalamotomy for moderate-to-severe tremor in Parkinson's disease. Parkinsons Dis Hindawi Publishing Corporation, 2015;2015:6–9.

Sokka SD, King R, Hynynen K. MRI-guided gas bubble enchanced ultrasound heating in in vivo rabbit thigh. Phys Med Biol 2003;48:223–241. [PubMed: 12587906]

Takegami K, Kaneko Y, Watanabe T, Maruyama T, Matsumoto Y, Nagawa H. Polyacrylamide gel containing egg white as new model for irradiation experiments using focused ultrasound. Ultrasound Med Biol 2004;30:1419–1422. [PubMed: 15582242]

Tran BC, Seo J, Hall TL, Fowlkes JB, Cain CA. Microbubble-enhanced cavitation for noninvasive ultrasound surgery. IEEE Trans Ultrason Ferroelectr Freq Control IEEE, 2003;50:1296–1304.

Tung YS, Liu HL, Wu CC, Ju KC, Chen WS, Lin WL. Contrast-agent-enhanced ultrasound thermal ablation. Ultrasound Med Biol 2006;32:1103–1110. [PubMed: 16829324]

Umemura S, Kawabata K, Sasaki K. In Vivo Acceleration of Ultrasonic Tissue Heating by Microbubble Agent. IEEE Trans Ultrason Ferroelectr Freq Control 2005;52:1690–1698. [PubMed: 16382620]

Yang X, Church CC. A model for the dynamics of gas bubbles in soft tissue. The Journal of the Acoustical Society of America 2005; 118:3595–606. [PubMed: 16419805]

Yu T, Fan X, Xiong S, Hu K, Wang Z. Microbubbles assist goat liver ablation by high intensity focused ultrasound. Eur Radiol 2006;16:1557–1563. [PubMed: 16541226]

Yu T, Wang G, Hu K, Ma P, Bai J, Wang Z. A microbubble agent improves the therapeutic efficiency of high intensity focused ultrasound: A rabbit kidney study. Urol Res 2004;32:14–19. [PubMed: 14655029]

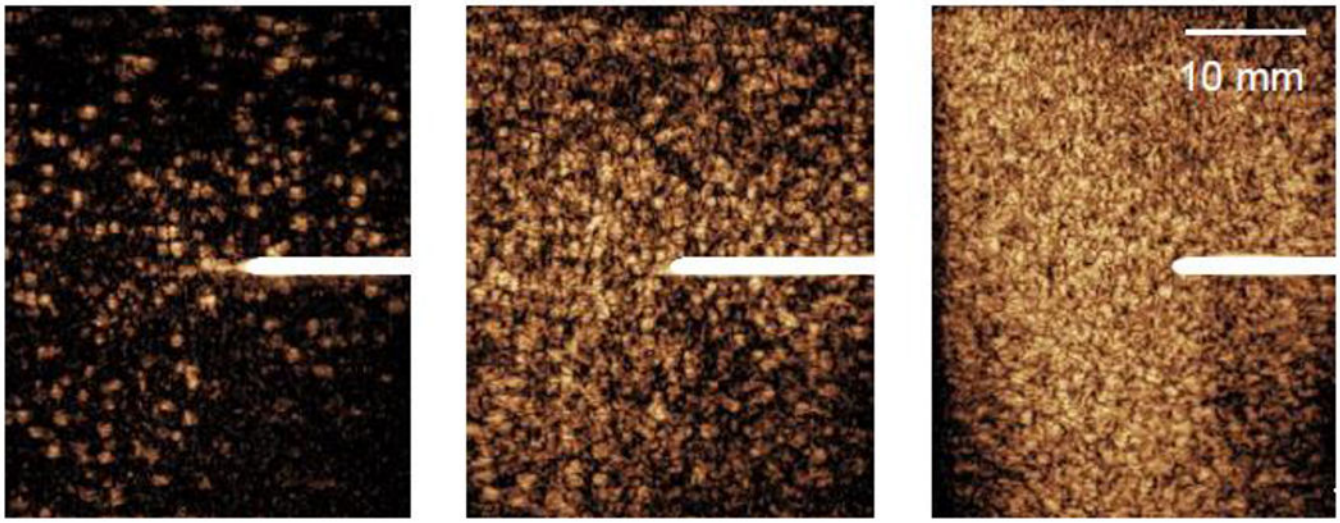

Figure 1:

Contrast-enhanced ultrasound images with the L9-3 linear array of the Philips iU22 showing the dilution of microbubbles in egg white phantoms at three different microbubble concentrations: (a) low (~10^2 MBs/mL), (b) medium (~10^3 MBs/mL), and (c) high (~10^4 MBs/mL). Thermocouples (white lines centered vertically) were inserted into each phantom to measure the temperature rise during each thermal treatment.

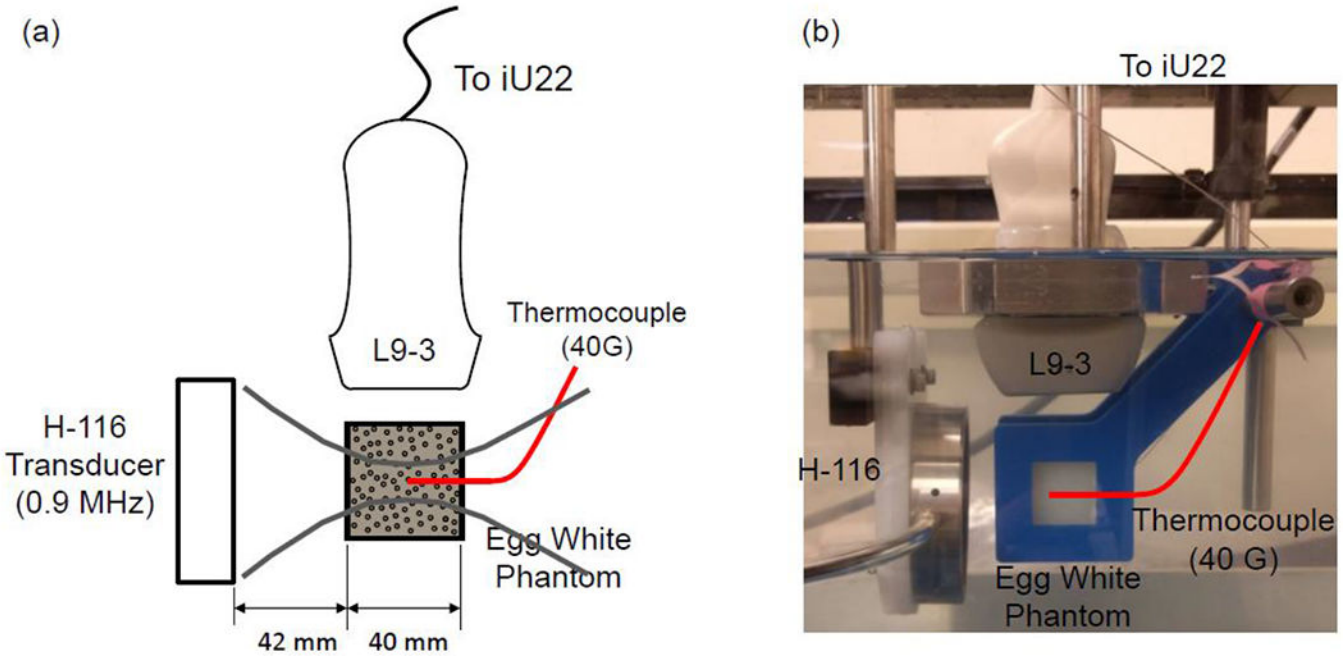

Figure 2:

Experimental setup. (a) Schematic of the H-116 transducer aligned with the inserted thermocouple. The thermocouple tip is aligned with the focus of the H-116 transducer. The imaging plane of the L9-3 imaging array is aligned with the axis of the H-116 transducer. (b) Photograph of the actual experimental setup.

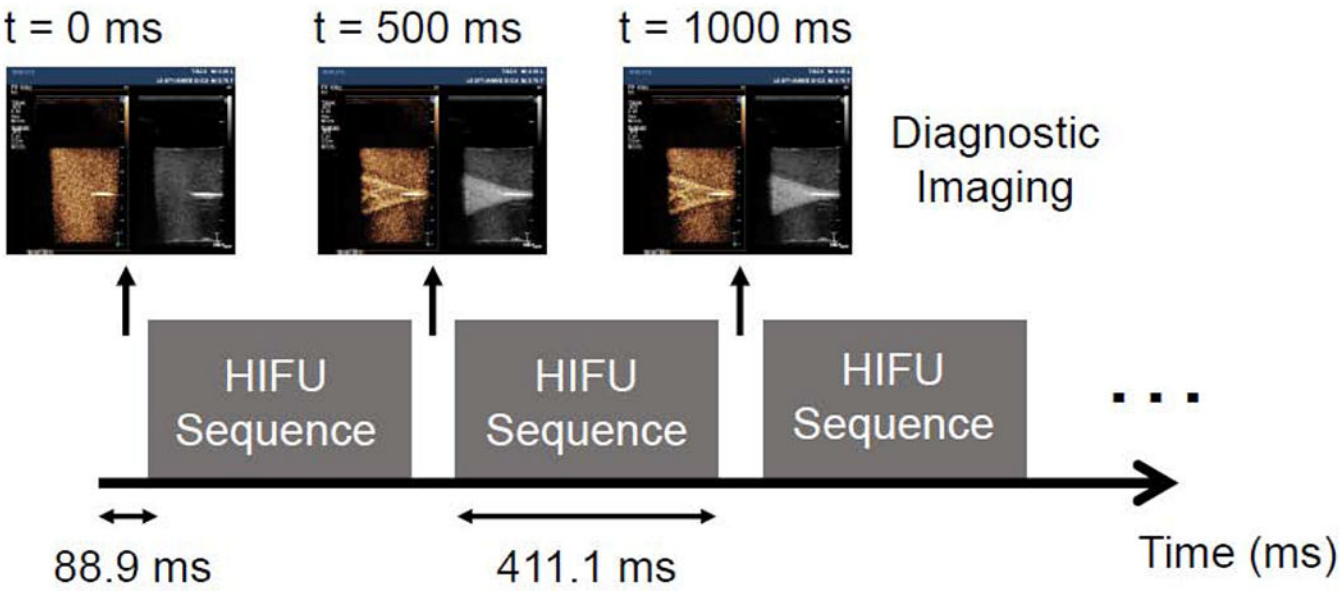

Figure 3:

Schematic showing the timing of the HIFU pulses and diagnostic imaging. Diagnostic imaging was interspersed with the HIFU pulse to allow real-time visualization of the treatment. The therapy transducer is turned on for 370,000 cycles (411.1 milliseconds) followed by a period where an ultrasound image is taken (88.9 milliseconds); this is repeated throughout the entire 30 second treatment.

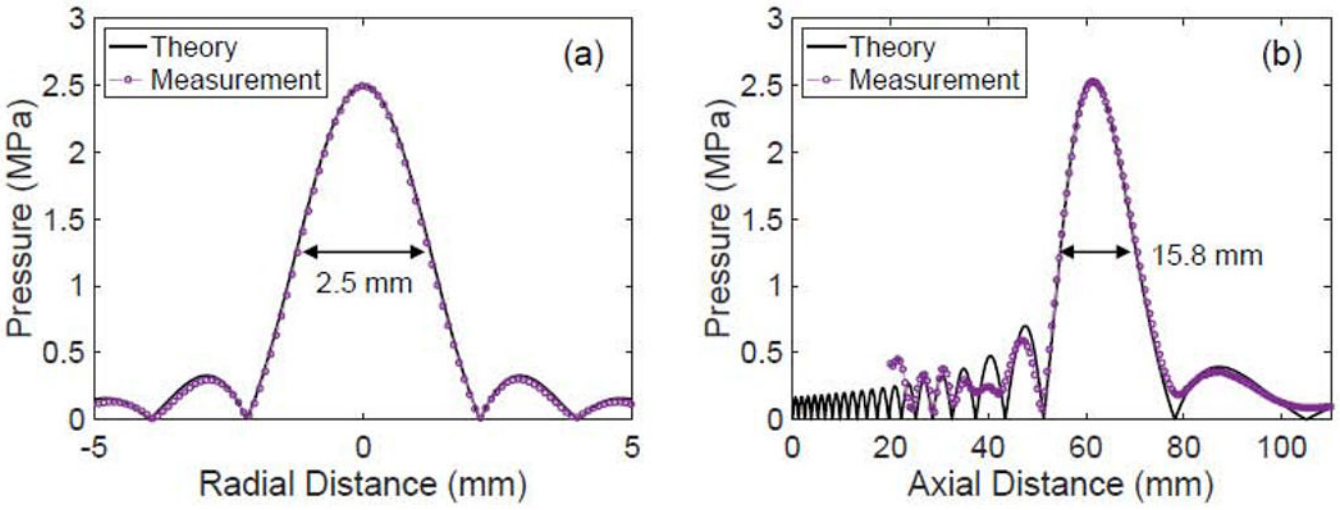

Figure 4:

Verification of the focal spot of the HIFU transducer. (a) Beam pattern taken at the focus of the transducer. The beam width (defined by the −6 dB points) at the focus is 2.5 mm. (b) Axial pressure field of the transducer. The axial beam width is 15.4 mm.

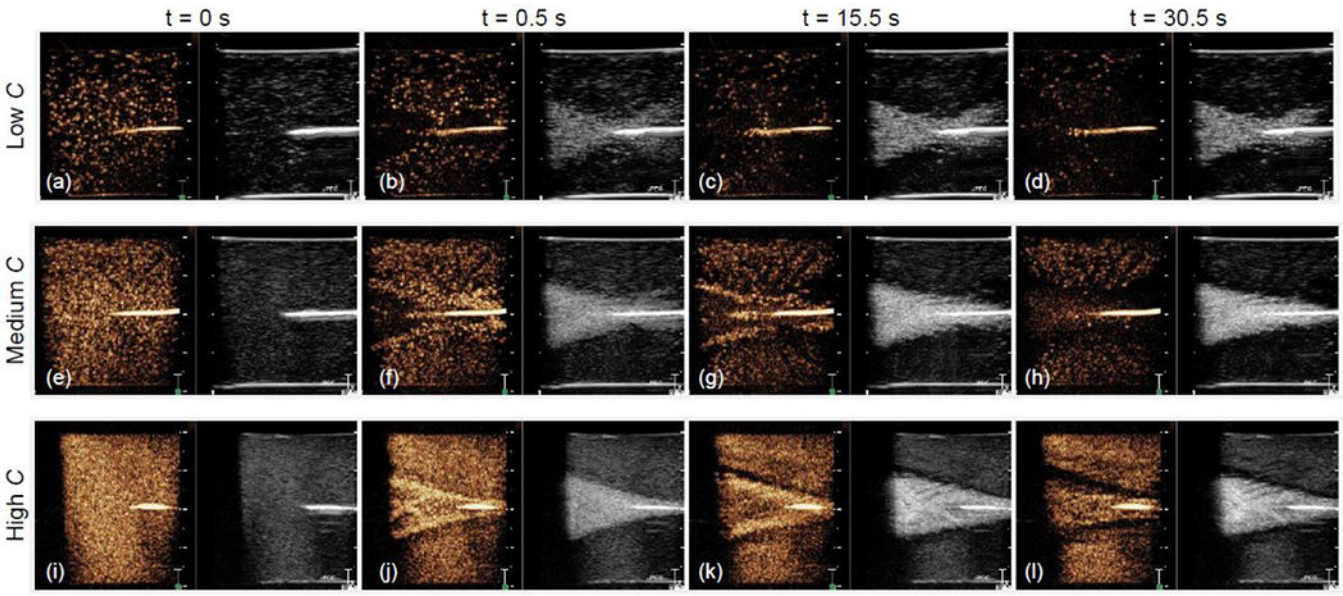

Figure 5:

Ultrasound images acquired during HIFU treatment at 2.0 MPa for three microbubble concentrations. The left-side orange-colored images are nonlinear contrast-enhanced ultrasound images (obtained with amplitude modulation) and the right-side greyscale images are conventional fundamental B-mode images. The echoes in the contrast images are produced by resonant nonlinearly oscillating microbubbles and in the B-mode images are produced by larger (not-resonant) bubbles produced during the HIFU treatment.

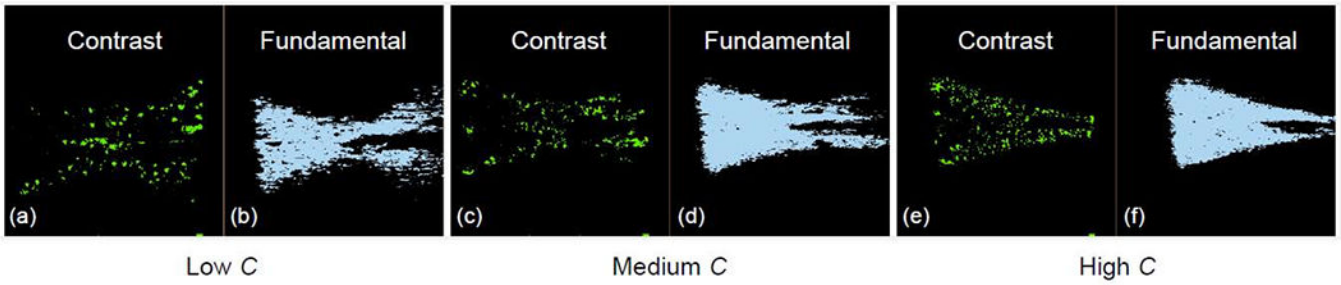

Figure 6:

Background-subtracted images showing the regions of the image with increased signal intensity between the image frame at the start of the treatment without ultrasound (t = 0 s) and the image frame taken immediately after the first ultrasound pulse (t = 0.5 s) at 2.0 MPa.

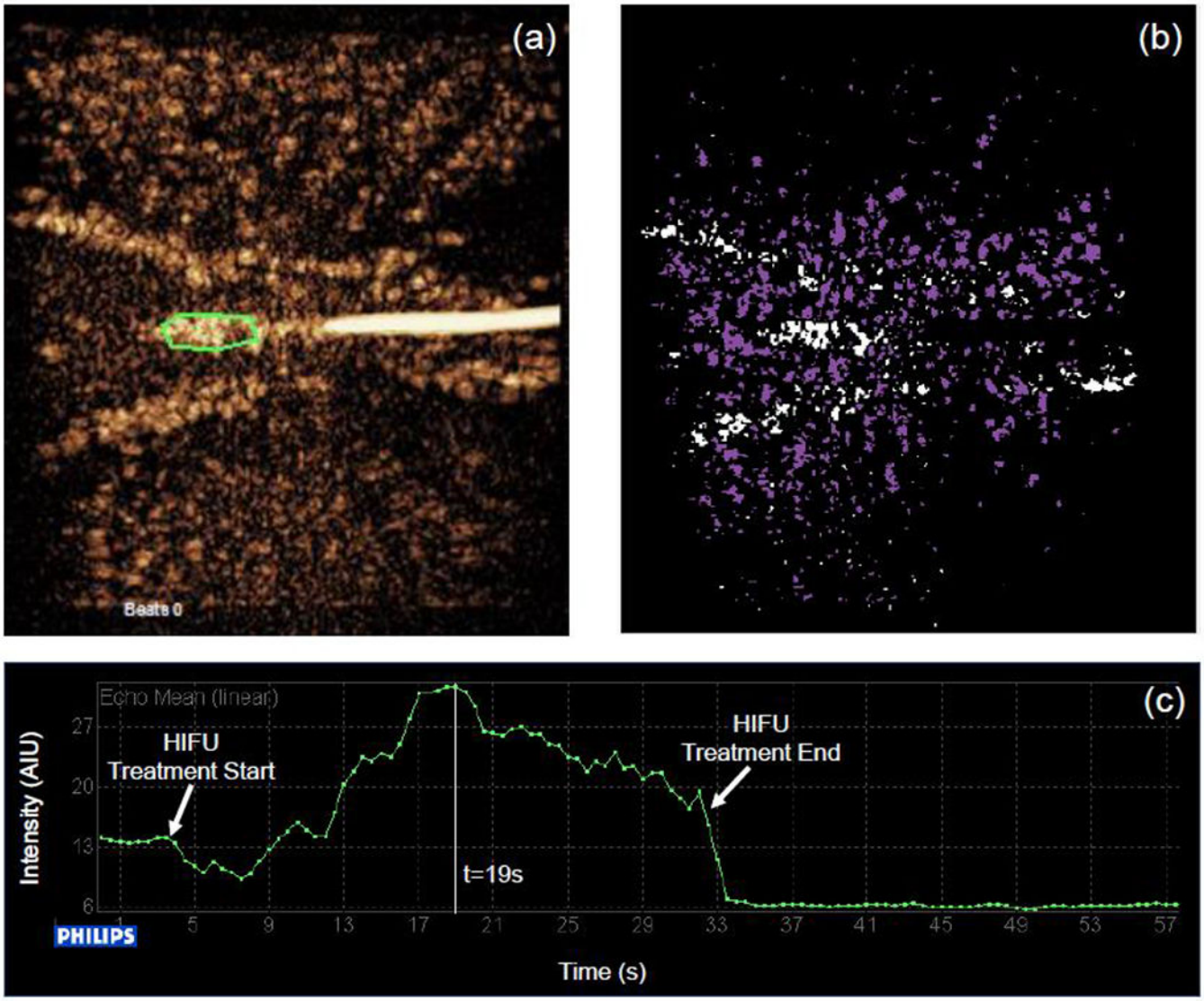

Figure 7:

(a) QLAB region of interest taken in the area of increased brightness directly in front of the thermocouple tip (outlined in green) in the contrast-enhanced ultrasound image for the medium concentration of microbubbles at 2.0 MPa. (b) Corresponding background subtracted contrast-enhanced ultrasound image showing the activated microbubbles (white) as well as the destroyed microbubbles (purple). (c) Time-intensity curve of a small region in front of the thermocouple where inertial cavitation takes place as a result of the HIFU pulse.

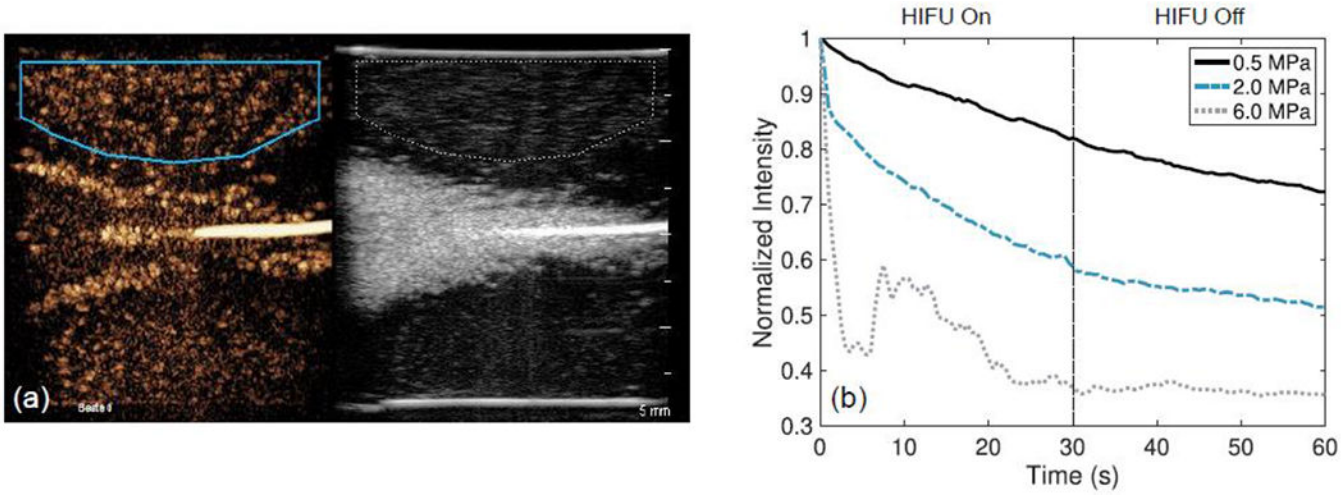

Figure 8:

QLAB region of interest analysis performed on DICOM loops for the medium concentration of microbubbles at 0.5 MPa (solid line), 2.0 MPa (dash-dotted line), and 6.0 MPa (dotted line). (a) Displays an example region of interest selected on the medium-concentration phantom treated at 2.0 MPa. (b) The image intensity in the region of interest over time.

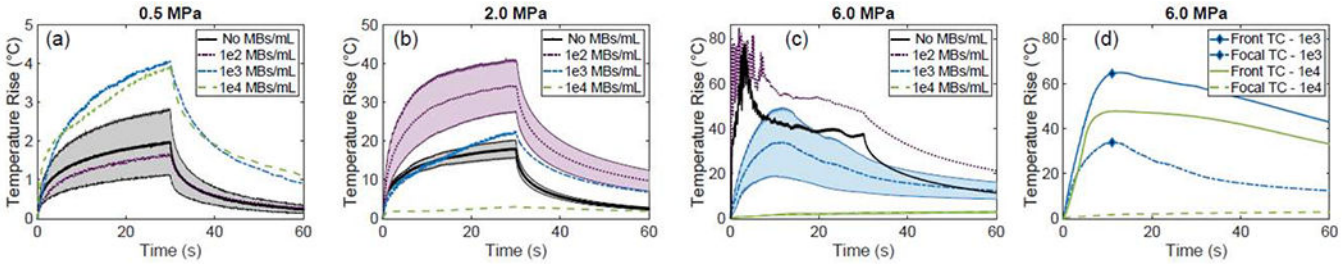

Figure 9:

Thermocouple temperature elevation measurements taken at the focus of the transducer in the phantom during the HIFU treatments (a)-(c), at 0.5 MPa, 2.0 MPa, and 6.0 MPa, respectively. Shaded areas show average value and standard deviation from a sample of 3 measurements. (d) Temperature elevation measurements taken from two thermocouples, one placed at the focus (dashed line) and one placed at the side of the phantom closest to the transducer (solid line), demonstrating that acoustic shadowing causes a higher temperature elevation proximal to the focus for the 2 higher bubble concentrations.

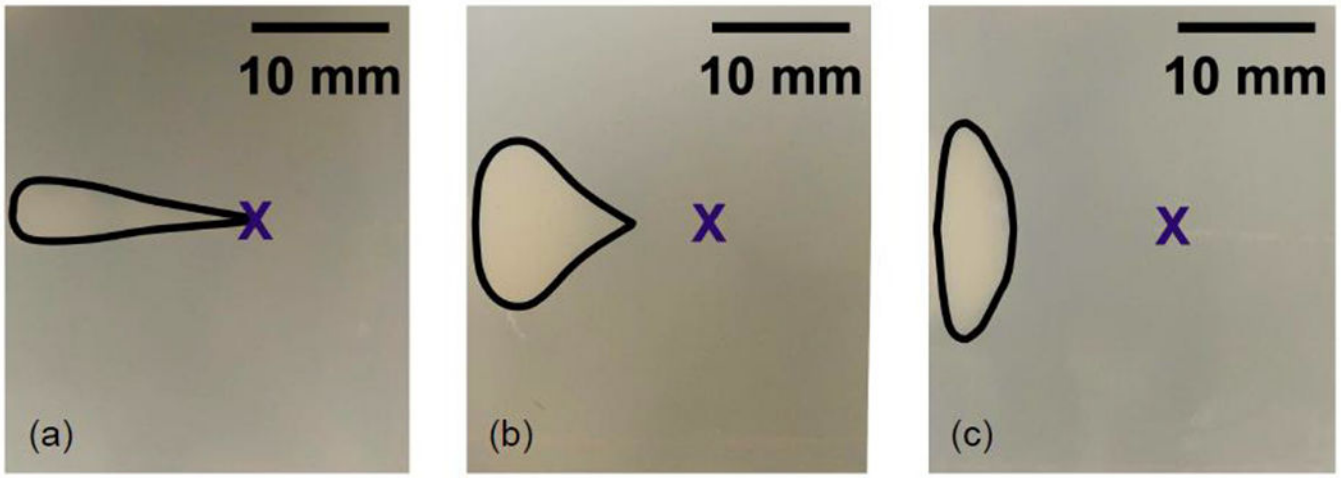

Figure 10:

Photographs of the phantom showing the lesion produced during HIFU exposure at 6 MPa, at low (a), medium (b), and high (c) microbubble concentration. The lesion shifts closer to the transducer (left side of images) as the concentration of microbubbles is increased due to attenuation of the sound field by the microbubbles. The **X** in the images marks the location of the focus.

Table 1:

Dilution of four types of microbubbles into egg white phantoms.

MB Type	Diluted into the Phantom
Bubble-G	X
Optison	X
Sonovue	✓
Sonazoid	✓✓

X: microbubbles do not survive the phantom preparation process. ✓: microbubbles survive the phantom process. ✓✓: microbubbles survive the phantom process and were selected for the experiments.